

## Mesopause temperatures derived from probing the hyperfine structure of the $D_2$ resonance line of sodium by lidar

K. H. FRICKE and U. VON ZAHN

Physikalisches Institut, Universität Bonn, Bonn, F.R.G.

(Received in final form 3 September 1984)

**Abstract**—In the 80–100 km altitude region free sodium atoms are abundant enough to allow the probing of the Doppler widened hyperfine structure (hfs) of the  $D_2$  resonance transition by ground-based lidar and hence to deduce atmospheric temperatures. We discuss the dependence of the observed shape of the hfs on the temperature, on geographic location and on polarization of the lidar, on differential extinction, and on the bandwidth of the lidar transmitter. The results are applied to new measurements of the mesopause sodium hfs structure obtained by the University of Bonn lidar.

### INTRODUCTION

The temperature in the 80–100 km altitude region of the terrestrial atmosphere has been derived in a number of ways. Typically temperatures are calculated by integration of the hydrostatic equation after obtaining *in situ* mass density data, either from drag observations or from mass spectrometers. Occasionally ion cluster concentrations combined with chemical equilibrium assumptions have been used to determine the atmospheric temperature from the known dependence of reaction rates on temperature. *In situ* measurements tend to be sparse, however, and are widely scattered in time and geographical location. Passive remote sensing methods utilize naturally occurring emissions from the atmosphere in several parts of the electromagnetic spectrum. These methods permit—in principle—continuous monitoring of the mesopause region temperature, but with little or no altitude resolution, which is readily available with *in situ* measurements. These techniques have recently been supplemented by active probing of the Doppler broadening of the hyperfine structure of the sodium  $D_2$  line by narrow-band lidar (light detection and ranging). This method promises to yield accurate temperature information combined with altitude resolution. It was first demonstrated by Thomas and co-workers (GIBSON *et al.*, 1979; THOMAS and BHATTACHARYYA, 1980).

Atomic sodium is present in the terrestrial upper atmosphere in the altitude range from about 80 to 100 km, with a peak density of several  $10^9$  atoms  $m^{-3}$ . The sodium  $D_2$  resonance line consists of six hyperfine transitions (Fig. 1). At atmospheric temperatures these six lines blend into two components, referred to as  $D_{2a}$  and  $D_{2b}$  (CHAMBERLAIN *et al.*, 1958), which are separated by about 2 pm. At a representative atmospheric temperature of 200K, Doppler broaden-

ing will produce a full width at half maximum (FWHM) of 1.2 pm, and thus the two components  $D_{2a}$  and  $D_{2b}$  are still resolved (Fig. 2). The minimum between them will be filled in only for temperatures in excess of 500K. Given a narrow-band, sufficiently powerful laser and a sensitive, high-speed detection system, one may probe this Doppler broadened hfs structure of the  $D_2$  line at

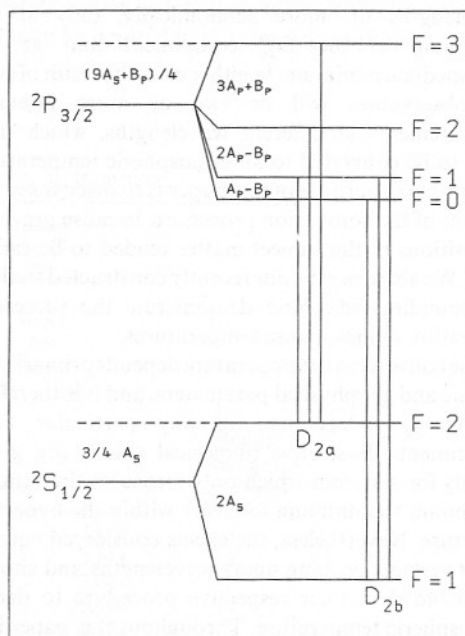


Fig. 1. Energy levels of  $^{23}\text{Na}$  connected by the  $D_2$  resonance line hfs multiplett.  $A_S$  and  $A_P$  are the dipole interaction constants for the S and P levels, respectively, and  $B_P$  is the quadrupole interaction constant. The separation of levels is not drawn to scale!

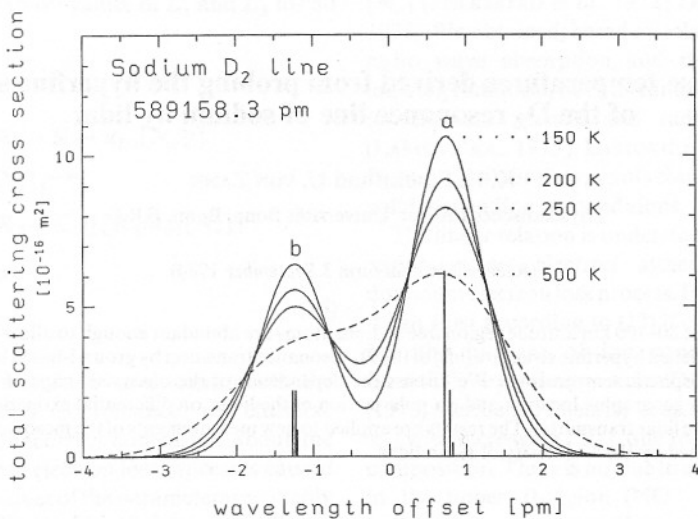


Fig. 2. Variation of the total scattering cross section in the Na hyperfine structure of the  $D_2$  resonance transition with atmospheric temperature.

several altitudes in the atmospheric sodium layer and thus derive height resolved temperatures between approximately 80 and 100 km. The probing of the hyperfine structure may be performed at several wavelengths or, more economically, only at the maximum of the  $D_{2a}$  component and at the intermediate minimum. In either case, the result of such an observation will be two or more intensity measurements at different wavelengths, which then need to be converted to an atmospheric temperature. The primary purpose of this paper is to discuss several aspects of the conversion procedure, because previous expositions of the subject matter tended to be rather brief. We also describe our recently constructed sodium hfs sounding lidar and demonstrate the successful derivation of mesopause temperatures.

The conversion to temperature depends primarily on atomic and geophysical parameters, and it is therefore reasonably independent of any particular lidar experiment. Illustrative numerical results are given mostly for a system which only measures the ratio of maximum to minimum intensity within the hyperfine structure. Nevertheless, the effects considered equally affect systems probing many wavelengths and should be included in their respective procedure to derive atmospheric temperature. Throughout this paper it is assumed that the transmitted beam is sufficiently diluted to ensure that induced transitions constitute only a negligible fraction. Appropriate quantitative expressions for the required experimental geometry have been derived by MEGIE *et al.* (1978).

#### ASPECTS OF THE CONVERSION PROCEDURE

##### *Wavelengths, relative amplitudes and lineshape*

In the atmospheric sodium layer the natural line shape is completely dominated by the Doppler effect. Postponing the inclusion of the instrumental linewidth until later, the backscattered signal  $S(\lambda, T)$  may be written as

$$S(\lambda, T) = C \sqrt{D/\pi T} \sum_{n=1}^6 A_n \exp[-D(\lambda - \lambda_n)^2/T], \quad (1)$$

where  $T$  is the atmospheric temperature and  $D = c^2 m / (2k\lambda_0^2) = 357.973 \pm 0.011 \text{ K pm}^{-2}$ . A single constant  $D$  for all six lines suffices (relative error about  $10^{-9}$ ). The constant  $C$ , which normalizes the theoretical function to the measured intensity, is irrelevant for the derivation of temperature, but will be discussed later in the context of sodium number densities. Besides temperature, the function  $S(\lambda, T)$  depends on 12 spectroscopic parameters, which are the relative intensities in the hyperfine structure multiplet  $A_n$  and the wavelengths  $\lambda_n$ , here measured as offset from the  $D_2$  transition wavelength  $\lambda_0$ . These parameters must be known independently to derive a temperature. In the following we collect reviewed atomic sodium parameters to determine  $\lambda_n$  and employ approximate resonance fluorescence theory for  $A_n$ .

The  $D_2$  resonance line of  $^{23}\text{Na}$ , which connects the  $^2S_{1/2}$  ground state to the  $^2P_{3/2}$  excited state, has a wave-

Table 1. Offsets for the D<sub>2</sub> hfs transitions

No.	<sup>2</sup> S <sub>1/2</sub>	<sup>2</sup> P <sub>3/2</sub>	Frequency (MHz)	Wavelength (pm)	
D <sub>2b</sub>	1	F = 1	F = 2	+1091.1 ± 0.2	-1.2633 ± 0.0002
	2		1	+1056.6 ± 0.3	-1.2234 ± 0.0004
	3		0	+1040.8 ± 0.4	-1.2051 ± 0.0005
D <sub>2a</sub>	4	F = 2	F = 3	-621.6 ± 0.2	+0.7197 ± 0.0002
	5		2	-680.5 ± 0.2	+0.7879 ± 0.0002
	6		1	-715.0 ± 0.3	+0.8279 ± 0.0004

length  $\lambda_0 = 589\ 158.26 \pm 0.07$  pm *in vacuo* (MARTIN and ZALUBAS, 1981). The nuclear angular momentum  $I = 3/2$ . The ground state splits into two hyperfine levels with total angular momentum quantum numbers  $F = 1$  and  $F = 2$ . The excited state has four hyperfine levels with  $F$  values ranging from 0 to 3 (see Fig. 1). The dipole interaction constants are  $A = 885.813\ 064$  MHz for the <sup>2</sup>S<sub>1/2</sub> and  $A = 18.69 \pm 0.09$  MHz for the <sup>2</sup>P<sub>3/2</sub> level. The quadrupole interaction constant for the <sup>2</sup>P<sub>3/2</sub> level is  $B = 2.90 \pm 0.21$  MHz (ARIMONDO *et al.*, 1977). The wavelength offsets  $\lambda_n$  with respect to  $\lambda_0$  for the allowed six transitions, calculated from these values of  $A$  and  $B$ , are listed in Table 1. The conversion factor from frequency to wavelength scale is  $-1.157\ 825\ 85$  pm/GHz at  $\lambda = 589$  nm. For the numbering of the lines we adopt the convention of THOMAS and BHATTACHARYYA (1980). The three lines

connecting to each of the two hfs levels of the ground state will blend once the temperature of the gas exceeds 6K; the resulting two components are referred to as D<sub>2a</sub> ( $F = 2$ ) and D<sub>2b</sub> ( $F = 1$ ).

In the geomagnetic field  $B$ , the hyperfine levels exhibit Zeeman splitting. As, in general, the transmitter of a lidar is polarized, the relative intensities are influenced via the selection rules for the magnetic quantum number  $m_F = 0, \pm 1$ . For fields of small magnitude the splitting is  $7.01 \cdot m_F \cdot B$  GHz for the ground level hfs states, where  $B$  is measured in Tesla, and the sign is negative for  $F = 1$  and positive for  $F = 2$ . For all of the hfs levels of the <sup>2</sup>P<sub>3/2</sub> state the magnitude of the splitting is  $6.67 \cdot m_F \cdot B$  GHz. In the geomagnetic field the energy level shifts will therefore not exceed 1.4 MHz, which is less than 0.3% of the hfs splitting and may be ignored in the conversion procedure.

Table 2. Relative intensities for D<sub>2</sub> hfs transitions

Site	Andøya	Bonn			
geogr. lat.	69°N	51°N			
geogr. long.	16°E	7°E			
magnetic field					
magnitude	51 μT	46 μT			
inclination	77°	66°			
polarization	circular	linear*			
pol.-alignment		north-south	east-west		
Transition	Relative intensities			Spatial average for multiplet	
D <sub>2b</sub>	1 (1-2)	5.074	4.935	5.102	5
	2 (1-1)	5.443	4.613	5.611	5
	3 (1-0)	2.030	1.974	2.041	2
D <sub>2a</sub>	4 (2-3)	15.449	12.736	15.996	14
	5 (2-2)	5.074	4.935	5.102	5
	6 (2-1)	1	1	1	1
Ratio D <sub>2a</sub> /D <sub>2b</sub>	1.715	1.620	1.733	1.6667	

\* The polarization the lidar at Bonn is hypothetical. It serves merely to demonstrate the magnitude of the Hanle effect.

However, the Zeeman splitting frequency is small compared to the inverse of  $2\pi$  times the lifetime of the excited state ( $16.40 \pm 0.03$  ns; GAUPP *et al.*, 1982), therefore the Hanle effect or zero-field level-crossing (HANLE, 1924; FRANKEN, 1961) will modify the spatial distribution of intensity. To illustrate the magnitude of the effect we evaluate the equations for the relative intensities, as given in the appendix, for our circularly polarized lidar stationed in northern Scandinavia and a hypothetical linear polarized one placed at Bonn with north-south and east-west alignment of the polarization direction. The results are compared to the WHITE and ELIASON (1933) multiplett intensity ratios in Table 2. Deviations from the spatially integrated ratios (5:5:2:14:5:1) as large as 10% may occur depending on geographic location and polarization of the lidar.

The twelve parameters  $A_n, \lambda_n$ , on which the function  $S(\lambda, T)$  depends, are known only with some errors  $\Delta A_n$  and  $\Delta \lambda_n$ . These errors will propagate and introduce an error  $\Delta S(\lambda, T)$  of magnitude

$$\Delta S(\lambda, T)^2 = \sqrt{\left(\frac{D}{\pi T}\right)} \sum_{n=1}^6 \left[ \left(\frac{\Delta A_n}{A_n}\right)^2 + \left(\frac{2D(\lambda - \lambda_n)\Delta \lambda_n}{T}\right)^2 \right] A_n^2 \exp\left(\frac{-2D(\lambda - \lambda_n)^2}{T}\right) \quad (2)$$

in the computed conversion curve. For a specific transition the contribution to the relative error by the uncertainty in wavelength will be about  $\{2D(\lambda - \lambda_n)/T\}\Delta \lambda$ , which at the intermediate minimum evaluates to  $\{2 \cdot 358 \cdot 1/200\}0.0005 = 4 \times 10^{-3}$ .

Inspection of Table 2 shows this error to be small compared to the changes of the relative multiplett intensities caused by the Hanle effect.

Figure 2 shows the variation of the scattering cross section with wavelength for three temperatures and Fig. 3 the ratio of maximum and minimum intensity  $R(T) = S(D_{2a}, T)/S(\lambda_{\min}, T)$  for several assumptions of geographic location and polarization of a lidar. We note also that the wavelength of the minimum shifts slightly with temperature. In terms of temperature the three conversion curves differ by  $\leq 6$ K for a 250K atmosphere, and the difference diminishes to 2.5K near 150K. The slopes near 150, 200 and 250K imply that for an accuracy in temperature of  $\pm 5$ K the intensity ratio needs to be measured with a relative error better than 7.3%; 4.5% and 2.8%, respectively.

#### Differential extinction

Inside the sodium layer the incoming and outgoing beams suffer equal amounts of extinction. If  $N$  is the column density of Na atoms from the bottom of the Na layer to the altitude under investigation, the total extinction is

$$E(\lambda, N) = \exp(-2\sigma_\lambda \cdot N), \quad (3)$$

where  $\sigma_\lambda$  is the wavelength dependent scattering cross section. The extinction will be larger for wavelengths with a higher observed intensity, consequently the observed ratio of maximum and minimum intensities will be smaller than for the case without differential

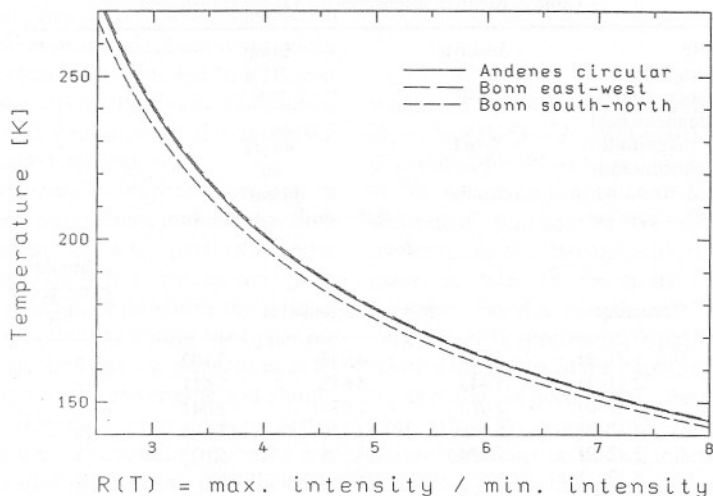


Fig. 3. Relationship between atmospheric temperature and ratio of intensity of the  $D_{2a}$  maximum and the intermediate minimum for a lidar station with different assumptions about the location and the state of polarization.

extinction and, hence, temperatures derived without correction will be higher than true atmospheric temperatures. To demonstrate the principle, we simplify matters by assuming that the traversed sodium column  $N$  is isothermal at the temperature of the altitude under investigation. Then  $R_{\text{cor}}$ , the ratio of the intensities corrected for extinction, is also the ratio of the scattering cross section. It is related to the observed ratio  $R_{\text{obs}}$  by

$$R_{\text{obs}} = R_{\text{cor}} \cdot \exp[-2\sigma_0 \cdot N \cdot (1 - 1/R_{\text{cor}})]. \quad (4)$$

Here the index 0 is given to the larger of the intensities, which would be the centre of the  $D_{2a}$  component in our numerical examples. The total scattering cross section at this centre is  $\sigma_{D_{2a}} = 1.303 \cdot 10^{-14} / \sqrt{T} \text{ m}^2$  in the Doppler regime, where  $T$  is given in Kelvin (see discussion on sodium number densities below). For assumed atmospheric temperatures of 150, 200 and 250K the differences between corrected and observed intensity ratios derived from the above formulated single scattering approximation are plotted in Fig. 4. Conversion scales to temperature are given on the right hand margin of the graph. Multiple scattering may in principle alleviate the situation, but even at the peak of the Na layer the photon free path

$$1/[\sigma_{D_2} \cdot n(\text{Na})] = 1/[10^{-15} \cdot 4 \cdot 10^9] = 250 \text{ km}$$

is large compared to the geometrical thickness of the sodium layer and much larger than typical transmitting (0.1 km) or receiving (1 km) beam diameters. The chance that a second scattering will return

a photon into the receiver beam is very small indeed. For column densities below about  $10^{13} \text{ m}^{-2}$  a correction for differential extinction will be less than 2K, but for column densities in excess of  $10^{14} \text{ m}^{-2}$  neglecting a correction may result in values of temperature systematically too large by more than 15K. Column abundances of this magnitude have been measured in the terrestrial mesopause region at least occasionally (HENRIKSEN *et al.*, 1980). The Na column densities required to perform the correction for differential extinction are of course obtained from the same measurement. These column density data need a corresponding correction for extinction (SIMONICH and CLEMESHA, 1983). In practical application, one would work slice by slice from the bottom to the top of the sodium layer and thus incorporate realistic temperature and density profiles.

#### Instrumental bandwidth and profile

A finite bandwidth of the laser will widen the apparent width of the  $D_{2a}$  and  $D_{2b}$  components and fill in the minimum in the observed intensity between them. Neglect of the transmitter profile will lead to temperatures that are systematically too high. The receivers in the Na-lidar systems have a much wider wavelength response than the separations of the hfs transitions and are presumed to have constant sensitivity over the hfs wavelength band. It is therefore sufficient to consider the influence of the bandwidth and profile of the transmitter on the derived atmospheric temperatures.

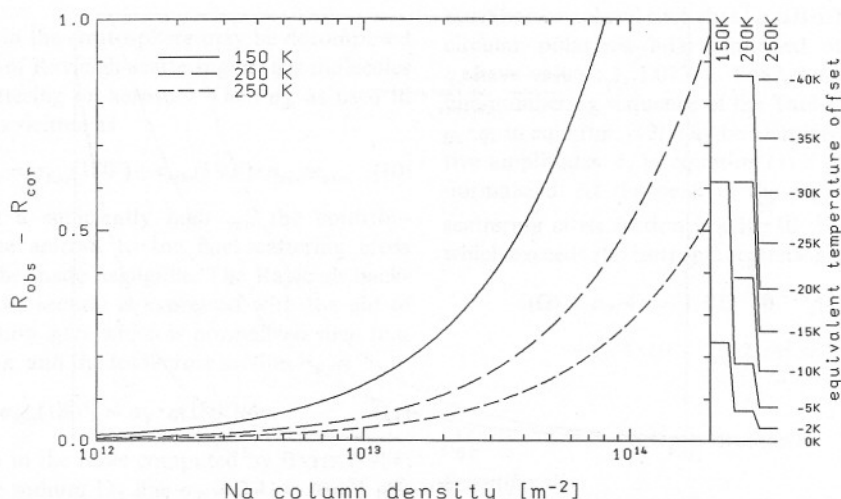


Fig. 4. Effect of differential extinction on observed intensity ratios for isothermal Na layers at 150, 200 and 250K and various column densities.

Let the wavelength profile of the transmitted laser pulses be given by the function  $p(\lambda)$ . The received signal  $S_c(\lambda, T)$  is the convolution of  $S(\lambda, T)$  and  $p(\lambda)$

$$S_c(\lambda, T) = \int S(\lambda, T) \cdot p(\lambda - \lambda') d\lambda'. \quad (5)$$

Assuming first that  $p(\lambda)$  is given by a Gaussian bell curve of full width at half maximum FWHM, then  $S_c(\lambda, T)$  will again be given by the Doppler type expression of equation (1), however, the apparent temperature  $T_a$  is larger than the true temperature  $T$  by

$$T_a - T = \frac{D \cdot \text{FWHM}^2}{4 \cdot (\ln 2)^2} = 186 \cdot \text{FWHM}^2 \quad (6)$$

where FWHM is to be measured in pm.

Next we consider the bandwidth limiting element in a lidar apparatus to be a Fabry-Perot interferometer (F.P.I.). From BORN and WOLF (1980; section 7.6, equations 15b, 21, 19, 42 and 46), we express the Airy function in terms of the full width at half maximum (FWHM), the free spectral range (FSR) and the wavelength offset  $\Delta\lambda$  from the centre of the bandpath

$$p(\Delta\lambda) = \frac{p(\text{centre})}{1 + \left[ \frac{2 \cdot \text{FSR}}{\pi \cdot \text{FWHM}} \sin\left(\frac{\pi \cdot \Delta\lambda}{\text{FSR}}\right) \right]^2} \quad (7)$$

$$\sim \frac{p(\text{centre})}{1 + \left[ \frac{2 \cdot \Delta\lambda}{\text{FWHM}} \right]^2 \cdot \left[ 1 - \frac{1}{3} \left( \frac{\pi \cdot \Delta\lambda}{\text{FSR}} \right)^2 \right]^2}. \quad (8)$$

In the approximation the sine function in the denominator of the Airy function was replaced by the first two terms of its series expansion. Clearly, if the second term may be dropped, the F.P.I. intensity distribution is of the Lorentz type. For the external F.P.I. in the Bonn lidar (FSR = 3.47 pm and FWHM = 0.13 pm), even at  $\Delta\lambda = 5 \cdot \text{FWHM}$  the Lorentz function will underestimate the Airy function by only 11%. If one assumes for the laser profile  $p(\lambda)$  a Lorentz type function, then the Doppler exponentials in equation (1) should be replaced by Voigt functions. As efficient algorithms for the Voigt function are available (HUI *et al.*, 1978, and references therein), the approximation of the laser line shape by a Lorentz type profile function offers considerable savings in the computation of the convolution (5).

In Fig. 5 we collect the curves which show the effect of the assumed profile  $p(\lambda)$  on calculated temperatures as a function of full width at half maximum for the case that the observed quantity is the ratio of maximum and minimum intensity  $R(T)$ . The line shapes tested are a Lorentz shape (which is also an approximation for a single F.P.I.), two F.P.I.s in series (with the FSR's of the external and intracavity etalons of the Bonn Lidar), and a Gaussian bell shape. For the F.P.I.s we took the FSR to remain constant, i.e. the variation in FWHM is thought to be affected by changes in the reflectivity of the F.P.I. mirrors. Expectedly, the correction is much larger for those profile functions which have extended wings in comparison with Gaussian bell curves. A knowledge of only the FWHM of the transmitted

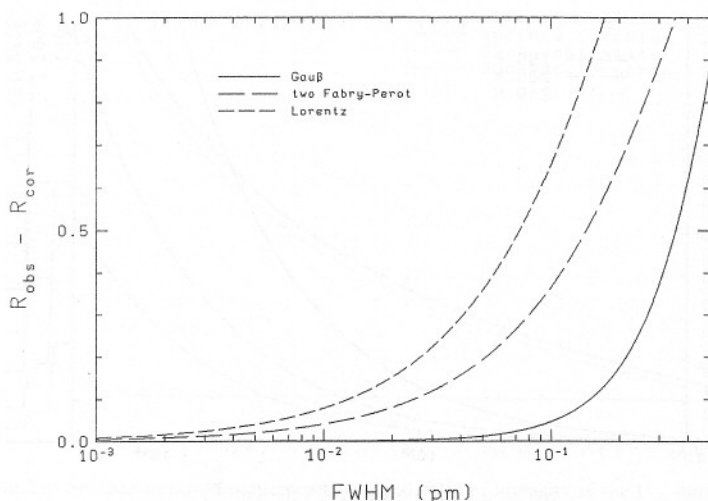


Fig. 5. The effect of the assumed instrumental profile function and its full width at half maximum on the derived atmospheric temperature.

pulses is insufficient unless this FWHM is smaller than approximately 0.01 pm; the magnitude of the wings need be known in order to perform a reliable calculation of the convolution (5).

### Sodium number densities

A lidar which is designed to measure mesopause temperatures is well equipped to determine sodium number densities. The narrow bandwidth of such a lidar eliminates the need to obtain an effective scattering cross section for the total sodium resonance line, as is required for the conventional wide-band lidar. Sodium number densities may be derived in principle if one knows the absolute transmitter power in the laser pulses, the time variable transmission of the atmosphere, which is determined mostly in the troposphere, and the absolute efficiency of the lidar receiver. In general, however, information about these quantities is poor, and it is often advantageous to eliminate them by normalizing the measurements to the backscattered signal from the stratosphere. Using the subscript Na for the sodium related quantities and the subscript St for those in the stratosphere, the sodium number density  $n_{\text{Na}}$  is

$$n_{\text{Na}}(z_{\text{Na}}) = n_{\text{St}}(z_{\text{St}}) \cdot \frac{\sigma(180^\circ)_{\text{St}}}{\sigma(180^\circ)_{\text{Na}}} \cdot \left[ \frac{z_{\text{Na}}}{z_{\text{St}}} \right]^2 \cdot \frac{I_{\text{Na}}}{I_{\text{St}}}, \quad (9)$$

where  $I_{\text{Na}}/I_{\text{St}}$  is the ratio of the observed count rates at any of the wavelengths  $\lambda$  to which the lidar is tuned. The square of the ratio of the altitudes  $z$  compensates for the variation of solid angle of the receiving telescope as  $z$  changes. The argument  $180^\circ$  on  $\sigma$  reminds us that the backscattering cross section is required. The atmospheric gas density in the stratosphere is denoted by  $n_{\text{St}}(z_{\text{St}})$ .

Scattering in the stratosphere may be decomposed into the sum of Rayleigh scattering on gas molecules and Mie scattering on aerosols. Then  $\sigma_{\text{St}}$  as used in equation (9) is written as

$$\sigma(180^\circ)_{\text{St}} = \sigma_{\text{Ray}}(180^\circ) + \sigma_{\text{Mie}}(180^\circ) \cdot n_{\text{aer}}/n_{\text{gas}}. \quad (10)$$

By choosing a sufficiently high  $z_{\text{St}}$ , the contribution from the aerosol to the backscattering cross section may be made negligible. The Rayleigh backscattering cross section is expressed with the aid of a phase function  $q(\Omega)$ , which is normalized such that  $\int q(\Omega) d\Omega = 4\pi$ , and the total cross section  $\sigma_T$  as

$$\sigma_{\text{Ray}}(180^\circ) = \sigma_T \cdot q(180^\circ)/4\pi. \quad (11)$$

Interpolation in the table computed by BATES (1984) yields for the sodium  $D_2$  line  $\sigma_T = 3.414 \cdot 10^{-31} \text{ m}^2$ . The author claims an accuracy of 1% for his tabulated values. At  $180^\circ$  we compute for the phase func-

tion  $q(180^\circ) = 300/203$ , where we have used the depolarization factor  $\delta \sim 0.03$  given by HANSEN and TRAVIS (1974) for air. Then equation (11) evaluates to  $\sigma_{\text{Ray}}(180^\circ) = 4.015 \cdot 10^{-32} \text{ m}^2 \text{ sr}^{-1}$ .

The density of gas molecules  $n_{\text{gas}}$  at altitude  $z_{\text{St}}$  is measured independently by meteorological radiosondes or is taken from appropriate model atmospheres if such data are not available.

Analogous to the above equation (11) we may express the backscattering cross section for sodium in terms of phase functions and spatially integrated total cross sections. The expression appears more complicated because six lines need to be added, which are normalised to the  $D_2$  oscillator strength  $f$  via the relative multiplet strength  $g_n$ , and the wavelength dependence must be included.

$$\sigma_{\text{Na}}(\Omega, \lambda) = \frac{\pi e^2}{mc} \cdot \frac{\lambda_0^2}{c} \cdot \frac{f}{\sum_n g_n} \cdot \sqrt{\frac{D}{\pi T}} \cdot \frac{1}{4\pi} \cdot \sum_n g_n q_n(\Omega) \exp[-D(\lambda - \lambda_n)^2/T]. \quad (12)$$

The symbols  $D$ ,  $T$  and  $\lambda_n$  were introduced in equation (1). Values for  $g_n$  are given in the last column of Table 2 with  $\sum g_n = 32$ . The oscillator strength of the Na  $D_2$  line is  $0.9536 \pm 0.0016$  (GAUPP *et al.*, 1982). We have not included the deviation from the ratio of statistical weights 2, which was observed by GAWLIK *et al.* (1979) to be 0.75%. The integrated absorption coefficient per atom for unit  $f$ -value  $\pi e^2/(mc) = \pi r_e c$ , where  $r_e$  is the classical electron radius, has value  $(2.654 002 \pm 0.000 009) \cdot 10^{-6} \text{ m}^2 \text{ s}^{-1}$  (COHEN and TAYLOR, 1973). The  $q_n(\Omega = 180^\circ)$  can be calculated from the equations given in the appendix, which must be normalized such that  $\int q_n(\Omega) d\Omega = 4\pi$ . For our circular polarized lidar stationed at Andøya the  $q_n$  have values: 1, 1.073, 1, 1.087, 1 and 0.985 in the line-numbering sequence of the Tables. The products  $g_n \cdot q_n$  in equation (12) may be identified with the relative amplitudes  $A_n$  in equation (1) if correspondingly normalized. At the peak of the  $D_{2a}$  line, the backscattering cross section is  $1.10 \cdot 10^{-15}/\sqrt{T} \text{ m}^2 \text{ sr}^{-1}$ , which exceeds the isotropic scattering value

$$\begin{aligned} \sigma(\Omega) &= \sigma_T/4\pi = 1.303 \cdot 10^{-14}/(4\pi\sqrt{T}) \\ &= 1.04 \cdot 10^{-15}/\sqrt{T} \text{ m}^2 \text{ sr}^{-1} \text{ by } 6\%. \end{aligned}$$

### THE INSTRUMENT

#### Scientific aim

At this point we remind the reader that the experiment under discussion aims at the measurement

of a geophysical parameter, the temperature in the mesopause region. Hence, the instrument employed for the measurement must be capable of operating over long time periods, it must be reasonably easy to align and to calibrate and preferably is of rugged design to permit the collection of data even from remote sites.

#### Measurement specifications

Our current knowledge of middle atmosphere structure and processes is such that it would considerably improve our understanding of these subjects if measurements of mesopause temperatures could be performed routinely having a temperature precision of less than 10K (which is equivalent to about 5% of typical mesopause temperatures) combined with an altitude resolution of at least 2 km. It is desirable to collect a number of such temperature profiles throughout one night, thus the integration time for a single profile should be less than 1 h. Furthermore, it would be hoped that the temperatures of the various altitude layers could be determined relative to each other with an accuracy considerably better than 10K.

Last, but not least, we emphasize that the three prime features, i.e. temperature accuracy, altitude resolution and integration time, can be traded against each other to a considerable extent.

#### Instrument layout

Basically, the instrument consists of: (1) a high-power, narrow-bandwidth, tunable laser system; (2) a receiving telescope; (3) a single-photon-counting multiplier; (4) fast pulse-counting electronics; (5) a reasonably fast computer for data processing and storage; (6) various calibration facilities for the absolute wavelength, the spectral shape and the energy of the laser pulses.

A schematic of the instrumental set-up is given in Fig. 6. The transmitter consists of a dye laser with an average pulse energy of 10 mJ and a repetition frequency of 10 Hz. A quarter wavelength plate is inserted into the beam path, which reduces back-coupling of the extracted beam into the oscillator and generates an almost circular polarized lidar transmitter beam. Its bandwidth is limited to about 0.13 pm FWHM by an

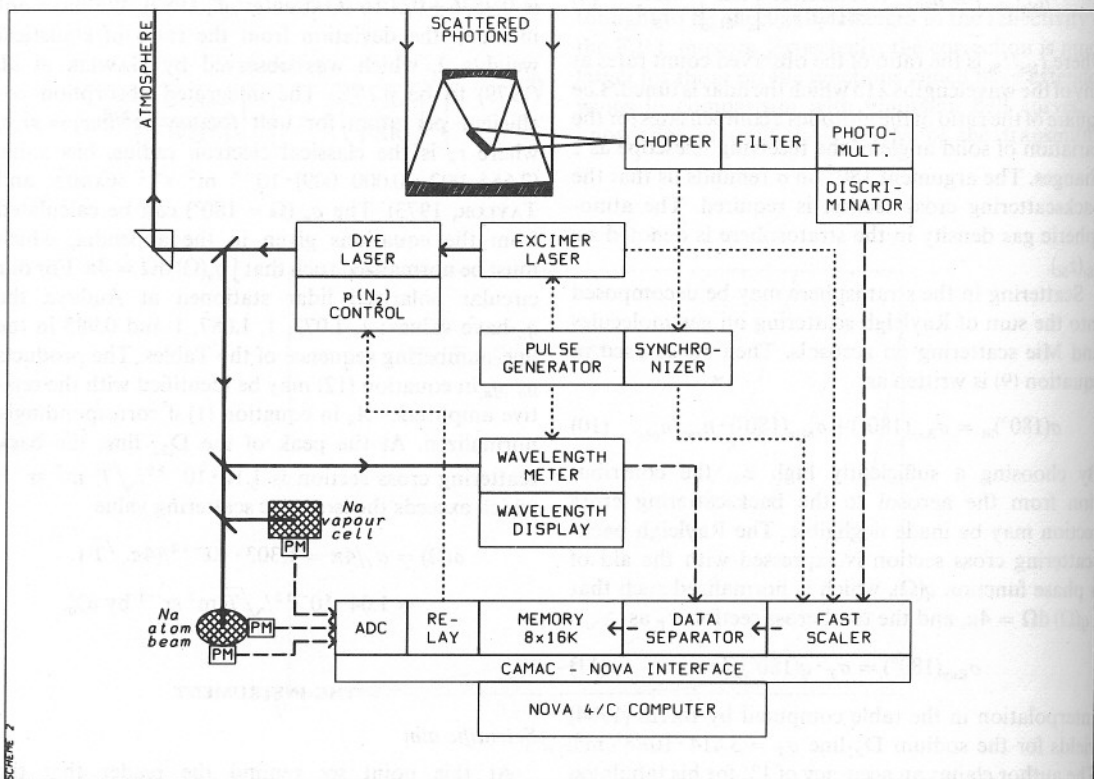


Fig. 6. Schematic of the Bonn University lidar system.

external, confocal Fabry-Perot. Fine tuning of the laser wavelength within the Na hfs is accomplished by varying (continuously or abruptly) the nitrogen pressure in the laser oscillator stage and the external F.P.I. Tuning the laser from the sodium  $D_{2b}$ - to the  $D_{2a}$ -component requires a pressure increase of 15 hPa. The dye laser is pumped by an excimer laser with pulse lengths of approximately 10 ns.

The dye laser does not have any feedback regulation of its wavelength. The latter jitters over a band of about  $\pm 0.1$  pm width during time periods of minutes. The wavelength of each laser pulse is, however, measured with a wavelength meter to a precision of 0.02 pm (or 1% of the wavelength distance between the sodium  $D_{2a}$ - and  $D_{2b}$ -components). The heart of the wavelength meter is a Fabry-Perot etalon of 5.8 pm FSR. Its interference rings are imaged onto a linear array of 100 photodiodes. After each laser pulse the charge states of the 100 diodes are read out into a single-board computer which calculates in less than 40 ms the desired wavelength information.

From time to time the absolute calibration of the wavelength meter and the spectral shape of the laser pulses are determined with the help of a sodium beam apparatus. The latter allows the almost Doppler-free excitation by the laser light of the 6 sodium hfs lines contributing to the Na  $D_2$ -transition. Their natural linewidth is 0.01 pm and they can therefore serve very well as standards for the wavelength meter calibration and as a tool to probe the much larger laser bandwidth.

A 1.5 m diameter searchlight mirror from World War II serves as primary mirror of the receiving telescope. Between the telescope and the photon-counting multiplier the light passes through a mechanical chopper, which protects the detector from the extremely strong backscatter signals originating from altitudes below 20 km. The chopper blades, having a diameter of 0.1 m, rotate with speeds up to  $650 \text{ rev s}^{-1}$ .

According to the information received from the wavelength meter, the data processing system assembles on-line all detected photons into a matrix of 30 wavelength bins (of approx. 0.075 pm each) and 180 altitude channels (of 0.5 km each), the latter depending on the round-trip time of the photons. After integration over an appropriate number of laser pulses these data are dumped onto a magnetic tape for later off-line processing. The entire instrument is mounted inside two standard  $2.4 \times 6$  m containers and is thus fully transportable.

#### Mesopause temperature profile

During the winter 1983/84 the instrument was positioned on the island of Andøya in northern Norway ( $69^\circ\text{N}$ ;  $16^\circ\text{E}$ ). To illustrate the performance of the

instrument in its present configuration we show in Fig. 7 data obtained during the night of 3 April 1984 between 21 h 06 m UT and 22 h 52 m UT from the altitude interval 90.5–91.5 km, which is near the altitude of the peak density in the sodium layer of that night. The general sky background, which includes time-variable auroral emissions and the photo-multiplier dark counts, was estimated from the signal assigned to the altitude intervals 60–75 km and 105–110 km and subtracted in each wavelength bin. The variation of the lidar transmitter energy, as well as the distribution of the emitted pulses in wavelength, were compensated for by normalizing the signal to the averaged signal from the stratosphere (20–40 km) in each wavelength bin. A mode structure from the laser oscillator was suppressed by averaging the signal in two adjacent, non-overlapping wavelength bins, which reduces the wavelength resolution to about 0.15 pm. This averaging process is simulated by a low order numerical Gaussian integration in the least squares fit procedure, which is used to derive an atmospheric temperature from equations (1) and (5) with the spectroscopic parameters listed in Tables 1 and 2 for Andøya. The spectral line shape of the laser was taken as Lorentzian with a FWHM = 0.15 pm, as determined by the monitor etalon before and during the data

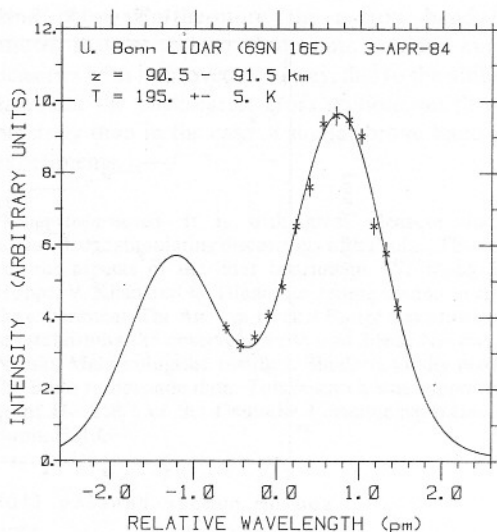


Fig. 7. Relative intensities from the  $D_{2a}$  component of the sodium hyperfine structure in the terrestrial atmosphere in the  $91 \pm 0.5$  km range observed (data points) on 3 April 1984 at Bleik ( $69^\circ\text{N}$ ,  $16^\circ\text{E}$ ) on Andøya Island. The solid line is the best fit of the Doppler widened line shape to the data. The convolution with the instrument profile function is included. It corresponds to an atmospheric temperature of 195K.

taking. The statistical error of the least squares fit, as estimated by the MINUIT procedure (JAMES and ROOS, 1975) contributes an error of  $\pm 5\text{K}$  to the derived temperature of  $195\text{K}$  in the  $1\text{ km}$  altitude interval near the peak of the sodium layer. The uncertainty of the laser bandwidth on the night of the measurement is believed to be not more than  $\pm 0.05\text{ pm}$ . This translates into a corresponding error in the derived absolute temperature of  $\pm 10\text{K}$ .

The altitude profile of the signal strength corrected for the inverse square dependence on distance is shown as the solid line in Fig. 8a. On this night the sodium layer was rather narrow with a layer width of only  $5\text{ km}$  at sodium densities of half the maximum value. Near the peak of the layer the signal was sufficiently large to obtain one temperature value for every kilometer, but as the signal decreases towards the boundaries of the layers, the integration interval had to be increased to  $6.5$  and  $5\text{ km}$  at the bottom and top ends, respectively, in order to determine a meaningful temperature value. The complete altitude profile of temperature is plotted in Fig. 8b. The statistical error in the derived temperatures is  $4\text{--}6\text{K}$ , except for the edge intervals, where this error increases up to  $10\text{K}$ . As the sodium column density on this night was only about  $3.1 \cdot 10^{13}\text{ m}^{-2}$ , we have not corrected the temperature for differ-

ential extinction towards the top end of the layer in view of the magnitude of the statistical error. The systematic error generated by the uncertainty in the line shape of the lidar transmitter (see above) needs to be added. The temperature profile in Fig. 8b clearly shows the mesopause temperature minimum and the steep temperature gradient towards the lower thermosphere, demonstrating that in the present configuration the Bonn lidar is capable of determining relative temperature profiles with a  $5\text{--}6\text{K}$  accuracy. We expect to be able to improve the accuracy once the oscillator of our dye laser has been improved to guarantee single-mode operation over long time periods.

On the same night and from the same site the  $\text{OH}^*$  spectrometer of the University of Wuppertal measured a rotational temperature of  $208.0 \pm 0.6\text{K}$  for the  $\text{OH}^*$  layer, which is believed to extend from  $82$  to  $90\text{ km}$  altitude (OFFERMANN, 1984). We note that there is excellent agreement for the temperatures which are derived by the passive  $\text{OH}^*$  remote sensing method and by active lidar probing of the sodium hyperfine structure in the altitude region of overlap.

#### Sodium number densities

Sodium number densities were calculated via normalisation to the stratosphere backscattered signal

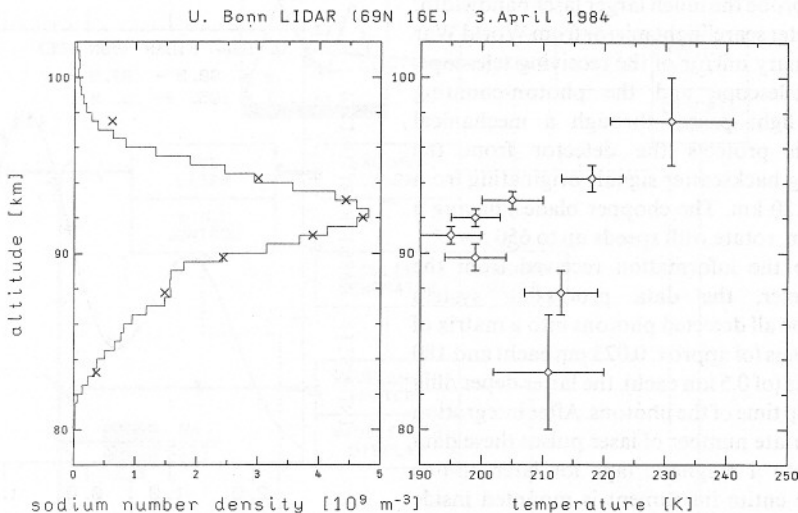


Fig. 8. Results obtained for 3 April 1984 between 21 h 06 m and 22 h 52 m UT at Andøya ( $69^\circ\text{N}$ ,  $16^\circ\text{E}$ ). The sodium layer was subdivided into eight slices of about equal signal strength to obtain comparable signal/noise ratios throughout the layer. (a) Average sodium number densities in each of the eight slices (crosses). These are based on comparison with the Rayleigh scattered signal from  $30\text{ km}$  altitude. The line is the solid angle corrected count rate, normalized to the sodium density in the  $91 \pm 0.5\text{ km}$  slice. Differences are mainly due to the different altitude resolution of the two datasets. (b) Mesospheric temperature profile. Note that the absolute value of the temperature scale is uncertain by about  $\pm 10\text{K}$  because of the remaining uncertainty in the lineshape of the lidar transmitter. Error bars in the figure show statistical errors from the fit procedure only.

Below about 25 km the lidar signal deviates from a smooth profile, which is expected for pure Rayleigh scattering on the atmospheric gas, and thus indicates the presence of additional Mie scattering centres. The stratosphere gas densities were derived from the regular 3 April 1984 midnight ascent from the radiosonde station at Bodø, Norway. This ascent is next in time to our lidar measurements, however, Bodø is situated about  $2.1^\circ$  in latitude to the south of the lidar site. The ascent reached a maximum altitude of 29.8 km and indicates an almost isothermal stratosphere at 221K above 25 km. We have chosen a normalizing altitude of 30 km, which requires slight extrapolation of the radiosonde data. At 30 km the ambient gas density is  $3.88 \cdot 10^{23} \text{ m}^{-3}$ . For each slice of the sodium layer for which we have derived temperatures, the column density of sodium atoms in this slice was calculated from equation (9) for each of the 14 wavelength bins (see Fig. 7), averaged and divided by the thickness of the slice. These slice-averaged sodium densities form the altitude profile plotted as crosses in Fig. 8a. The solid angle corrected signal, which shows the full altitude resolution of our lidar experiment, was normalized to the density of the 91 km slice (line in Fig. 8a). Adding the column densities of all slices yields a column density of  $3.1 \cdot 10^{13} \text{ m}^{-2}$  for the sodium layer.

The radiosonde intercomparison (SONDEX) that was conducted at Payerne, Switzerland, in April 1981 as part of the Alpine Experiment (ALPEX) shows that radiosonde pressure measurements have a precision of not better than 1.5 hPa (RICHNER and PHILLIPS, 1982). At our normalizing altitude of 30 km the pressure is about 12 hPa. The quality of the radiosonde pressure data presently dominates the relative error in our derived sodium densities.

#### SUMMARY

Active remote probing of the hyperfine structure of the  $D_2$  transition of sodium in the 80–100 km region of the terrestrial atmosphere has recently become available as a tool for measuring the temperature profiles in a notoriously inaccessible volume of the atmosphere. The conversion of the observed intensities

to temperature depends on a theoretical calculation involving atomic and geophysical parameters. Comparing the lifetime of the excited state of the sodium atom and the hfs Zeeman splitting shows that the experiment is conducted in the regime of the zero-field level-crossing (Hanle effect) and thus the relative line strength entering the theoretical calculations will depend on the state of polarization of the lidar, as well as on the angle of the exciting and detecting beams with the geomagnetic field, i.e. on geographic location. The effect on the derived temperature amounts to a systematic shift of up to 5K. Differential extinction will modify the relative intensities of the observed backscattered light from different wavelengths within the hyperfine structure in such a way that apparent (uncorrected) temperatures are higher than true temperatures. A correction is necessary for sodium column densities larger than a few  $10^{13} \text{ m}^{-2}$ , i.e. frequently towards the top of the sodium layer. The finite bandwidth of the lidar transmitter acts so as to increase apparent temperatures. The correction is sensitive to the true wavelength profile up to several FWHM from the central transmitted wavelength. The newly constructed Bonn University Na-lidar is described, which is used to probe the Doppler-widened hyperfine structure of sodium atoms with its narrow-band laser. It is demonstrated that from the data obtained, altitude resolved mesopause temperatures can be derived in the 80–100 km region of the terrestrial atmosphere. Furthermore, the narrow band laser allows the derivation of absolute sodium number densities with improved accuracy, due to the ability to calculate the backscatter cross sections much more precisely than in the case of similar broad band lidar experiments.

*Acknowledgements*—It is with great pleasure that we acknowledge stimulating discussions with Prof. L. Thomas on various aspects of the lidar instrument. We thank U.-P. Hoppe, V. Klein and C. Tilgner for setting up and operating the experiment. The Andøya Rocket Range was most helpful in establishing the observation site near Bleik, Norway. Det Norske Meteorologiske Institutt, Blindern, kindly provided the Bodø radiosonde data. This research was supported by grant Ho 858/1 of the Deutsche Forschungsgemeinschaft, Bonn, F.R.G.

#### REFERENCES

- |  |      |   |
|--|------|---|
| ARIMONDO E., INGUSCIO M. and VIOLINO P.        | 1977 | <i>Rev. mod. Phys.</i> <b>49</b> , 31.                              |
| BATES D. R.                                    | 1984 | <i>Planet. Space Sci.</i> <b>32</b> , 785.                          |
| BORN M. and WOLF E.                            | 1980 | <i>Principles of Optics</i> , 6th Ed. Pergamon Press, Oxford, 1980. |
| CHAMBERLAIN J. W., HUNTEN D. M. and MACK J. E. | 1958 | <i>J. atmos. terr. Phys.</i> <b>12</b> , 153.                       |
| COHEN E. R. and TAYLOR B. N.                   | 1973 | <i>J. phys. chem. Ref. Data</i> <b>2</b> , 663.                     |
| FRANKEN P. A.                                  | 1961 | <i>Phys. Rev.</i> <b>121</b> , 508.                                 |

- GAUPP A., KUSKE P. and ANDRÁ H. J. 1982 *Phys. Rev.* **A26**, 3351.  
 GAWLIK W., KOWALSKI J., NEUMANN R. 1979 *J. Phys. B, atom. molec. Phys.* **12**, 3873.  
 WIEGEMANN H. B. and WINKLER K.  
 GIBSON A. J., THOMAS L. and BHATTACHARYYA S. K. 1979 *Nature* **281**, 131.  
 HANLE W. 1924 *Z. Phys.* **30**, 93.  
 HANSEN J. E. and TRAVIS L. D. 1974 *Space Sci. Rev.* **16**, 527.  
 HENRIKSEN K., SIVJEE G. G. and DEEHR C. S. 1980 *J. geophys. Res.* **85**, 5153.  
 HUI A. K., ARMSTRONG B. H. and WRAY A. A. 1978 *J. quant. Spectrosc. radiat. Transfer* **19**, 509.  
 JAMES F. and ROOS M. 1975 *Comput. Phys. Commun.* **10**, 343.  
 MARTIN W. C. and ZALUBAS R. 1981 *J. phys. chem. Ref. Data* **10**, 153.  
 MEGIE G., BOS, F., BLAMONT J. E. 1978 *Planet. Space Sci.* **26**, 27.  
 and CHANIN M. L.  
 RICHTER H. and PHILLIPS P. D. 1982 *Pure appl. Geophys.* **120**, 852.  
 SIMONICH D. M. and CLEMESHA B. R. 1983 *Appl. Optics* **22**, 1387.  
 THOMAS L. and BHATTACHARYYA S. K. 1980 *Proceedings of the Vth ESA-PAC Symposium on European Rocket and Balloon Programmes and Related Research*, ESA SP-152, p. 49.  
 WHITE H. E. and ELIASON A. Y. 1933 *Phys. Rev.* **44**, 753.  
 ZIMMERMANN D. 1975 *Z. Phys.* **A275**, 5.
- Reference is also made to the following unpublished material:  
 OFFERMANN D. 1984 Private communication.

## APPENDIX

*Relative intensities of the hfs lines for the Na D<sub>2</sub> resonance line in a lidar geometry*

Because of the polarization of the lidar transmitter and the magnitude of the geomagnetic field, interferences in the resonantly scattered light should be considered in the calculations of the relative amplitudes of the hyperfine transitions (Hanle effect or zero-field level-crossing; HANLE, 1924; FRANKEN, 1961). In this section we apply equations (6) and (8) of ZIMMERMANN (1975) to a Na lidar situation. These equations cover the Zeeman coherences within a single hfs level, but neglect interference terms between sublevels belonging to different ones. The validity is limited to weak magnetic fields such as the Earth field. The resonance fluorescence intensity may be written as a sum of products of the reduced matrix elements (identical for the six hfs transitions), the relative intensities of the hfs lines, and a geometrical factor (the product of the polarization tensors for the exciting and the observing beams).

The relative intensities evaluated from equation (6) of ZIMMERMANN (1975) are (note that a common factor of 1/96 was removed):

No.	Transition	Relative intensity	Integral
1	$F = 1$ to $F = 2$	$5 \cdot \Sigma(0) - 5/2 \cdot \Sigma(1)$	$40\pi/3$
2	$F = 1$	$5 \cdot \Sigma(0) - 5/6 \cdot \Sigma(1) + \Sigma(2)$	$40\pi/3$
3	$F = 0$	$2 \cdot \Sigma(0)$	$16\pi/3$
4	$F = 2$ to $F = 3$	$14 \cdot \Sigma(0) - \sqrt{(2352/175)} \cdot \Sigma(1) + 84/25 \cdot \Sigma(2)$	$112\pi/3$
5	$F = 2$	$5 \cdot \Sigma(0) - 5/6 \cdot \Sigma(1)$	$40\pi/3$
6	$F = 1$	$1 \cdot \Sigma(0) + 1/6 \cdot \Sigma(1) - 1/25 \cdot \Sigma(2)$	$8\pi/3$

where  $\Sigma(k) = \sum_{q=-k}^{+k} (-1)^{k+q} \cdot \Phi(k; -q, q)/(1 + i \cdot g_F \cdot q \cdot y)$  and  $i = \sqrt{-1}$ ,  $g_F = 2/3$  the Landé  $g$ -factor for the  $P_{3/2}$  state and  $y = \mu_{\text{Bohr}} \cdot \tau \cdot B/\hbar$ . Using, from COHEN and TAYLOR (1973), for the Bohr magneton  $\mu_{\text{Bohr}} = 9.27408 \cdot 10^{-24} \text{ J T}^{-1}$  and the Planck constant  $\hbar = h/2\pi = 1.054589 \cdot 10^{-34} \text{ J s}$  and for the lifetime of the  $^2\text{P}$  state of sodium  $\tau = 16.40 \pm 0.03 \text{ ns}$

(GAUPP *et al.*, 1982), we find  $y = 1.442 \cdot 10^3 B$ , where the geomagnetic field strength is measured in units of Tesla. Typically  $y$  ranges from 0.04 to 0.1 for values of the Earth field.

The viewing geometry and state of polarization of the transmitter and receiver are described by  $\Phi(k; -q, q)$ , which abbreviates the product  $\Phi(k; q; \mathbf{e}) \cdot \Phi(k; q; \mathbf{u})$  in equation (6) of ZIMMERMANN (1975). By referring to Fig. A1 one can relate the angles  $\theta$  and  $\phi$  used by Zimmermann to the angle  $\chi$  between the direction of light propagation and the direction of the geomagnetic field vector. For the transmitted lidar beam  $\theta = \chi$ , for the receiving beam  $\theta = 180 - \chi$ , and for both beams  $\phi = 0$ . The unit vectors  $\theta_0$  and  $\phi_0$  in the plane perpendicular to the direction of propagation are used to describe the state of polarization. For the transmitted beam  $\theta_0$  is directed towards geomagnetic south and  $\phi_0$  towards magnetic east. The directions reverse for the receiving beam. Referring again to ZIMMERMANN's (1975) notation, circular polarization is described by  $\gamma = \pm 90^\circ$ , and linear by  $\gamma = 0^\circ$ . The direction of linear polarization is given by  $\alpha$  with respect to the magnetic north-south direction. It relates to  $\beta$  in ZIMMERMANN (1975) by

$\alpha = \beta/2$ . In general the receiver will not be sensitive to polarization, hence we add either right and left circular polarized light or, equivalently, two perpendicularly linear polarized beams.

The resulting geometrical factors for a circular polarized lidar transmitter, as well as an unpolarized one, in

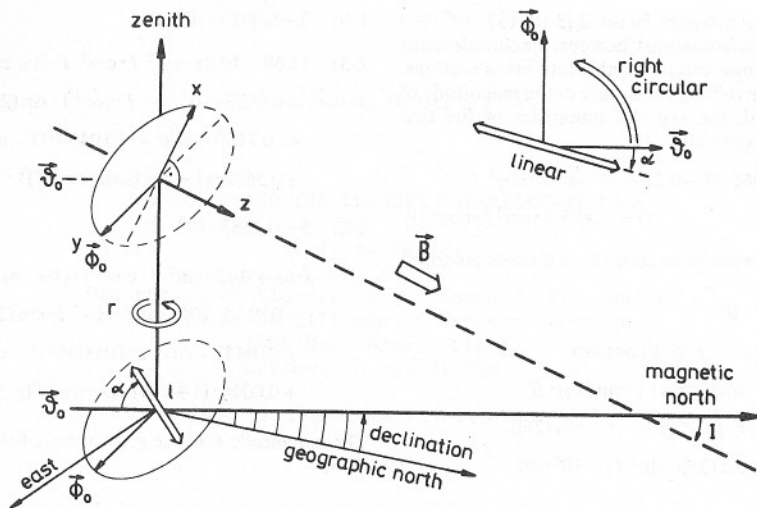


Fig. A1. Oblique view downward on a lidar observation geometry. The plane through the lidar beams and the magnetic field vector coincides with the  $x-z$  plane of the coordinate system used for describing the scattering process. The  $y$  direction is horizontal. The unit vector  $\phi_0$  is parallel to  $y$ . The inset presents a view in the nadir direction (into the laser beam) and defines the coordinates used for describing the state of polarization of the transmitter beam.

combination with a receiver insensitive to polarization are:

$k$	$-q$	$q$	$\Phi(k; -q, q)$
0	0	0	2/3
1	all $q$	all $q$	0
2	-2	+2	$1/8 \cdot \sin^4 \chi$
	-1	+1	$1/2 \cdot (\sin \chi \cdot \cos \chi)^2$
	0	0	$1/3 - \sin^2 \chi + 3/4 \cdot \sin^4 \chi$
	1	1	$1/2 \cdot (\sin \chi \cdot \cos \chi)^2$
	2	-2	$1/8 \cdot \sin^4 \chi$

direction and of the polarization, reproduces the usually quoted relative multiplett intensities as found in the WHITE and ELIASON (1933) tables.

In a typical lidar set-up, the transmitting and receiving beams point into the local zenith. Then the angle  $\chi$  between the beam and magnetic field vector directions is related to the inclination  $I$  of the geomagnetic field by  $\chi = I + 90^\circ$ . Further, if one neglects terms involving the cube and higher powers of the magnitude of the magnetic field in the above sums, one generates an error of less than 0.5% in the relative intensities of the 6 hfs lines. With these approximations the above equations reduce to the following.

If the transmitter is linearly polarized, again with a receiver insensitive to polarization, then the geometrical factors are:

$k$	$-q$	$q$	$\Phi(k; -q, q)$
0	0	0	2/3
1	all $q$	all $q$	0
2	-2	2	$\sin^2 \chi \cdot [(\sin \chi \cdot \cos \alpha)^2 - \cos(2\alpha) - i \cdot \cos \chi \cdot \sin(2\alpha)]/4$
	-1	1	$\sin^2 \chi \cdot \cos \chi \cdot [\sin \chi \cdot \cos^2 \alpha + i \cdot \sin \alpha \cdot \cos \alpha]$
	0	0	$1/3 - 1/2 \cdot \sin^2 \chi (2 + \cos(2\alpha)) + 3/2 \cdot \sin^4 \chi \cdot \cos^2 \alpha$
	1	-1	$\sin^2 \chi \cdot \cos \chi \cdot [\sin \chi \cdot \cos^2 \alpha - i \cdot \sin \alpha \cdot \cos \alpha]$
	2	-2	$\sin^2 \chi \cdot [(\sin \chi \cdot \cos \alpha)^2 - \cos(2\alpha) + i \cdot \cos \chi \cdot \sin(2\alpha)]/4$

(a) Transitions and relative intensity for a circular polarized lidar, as well as an unpolarized lidar.

1-2:	$5 + 0.2283 \cdot 10^8 \cdot B^2$
1-1:	$5.5 - 3 \cdot \sin^2 I \cdot \cos^2 I + (0.2511 - \cos^2 I - (0.0137 + 0.1096 \cdot \sin^2 I)) \cdot 10^8 \cdot B^2$
1-0:	$2 + 0.0913 \cdot 10^8 \cdot B^2$
2-3:	$15.68 - 10.08 \cdot \sin^2 I \cdot \cos^2 I + (0.7160 - \cos^2 I - (0.0460 + 0.3682 \cdot \sin^2 I)) \cdot 10^8 \cdot B^2$
2-2:	$5 + 0.2283 \cdot 10^8 \cdot B^2$
2-1:	$0.98 + 0.12 \cdot \sin^2 I \cdot \cos^2 I + (0.0447 + \cos^2 I - (0.0005 + 0.0044 \cdot \sin^2 I)) \cdot 10^8 \cdot B^2$

The spatial integral over all emitting directions  $\mathbf{u}$  of  $\Sigma(0)$  is  $8\pi/3$ , and those over  $\Sigma(1)$  and  $\Sigma(2)$  are zero. The ratio of the coefficients of  $\Sigma(0)$ , which is independent of the propagation

where, additionally, a common factor  $2/(3+0.137 \cdot 10^8 \cdot B^2)$  has been removed. This factor must, however, be considered in the normalisation if one computes absolute cross sections. Dropping the terms involving the square of the magnitude of the geomagnetic field, the ratio of intensities of the two components is approximately

$$D_{2a}/D_{2b} = 5/3 \cdot 1.03968 \cdot (1 - 0.219834 \cdot \sin^2 I \cdot \cos^2 I \cdot (1 + 0.50202 \cdot \sin^2 I \cdot \cos^2 I)).$$

(b) *Transitions and relative intensity for a linearly polarized lidar.*

$$1-2: 5 + 0.2283 \cdot 10^8 \cdot B^2$$

$$1-1: 5.5 - 3 \cdot \sin^2 I \cdot \cos^2 I \cdot (1 + \cos(2\alpha)) \\ + 0.2867 \cdot 10^4 \cdot \sin I \cdot \cos^2 I \cdot \sin(2\alpha) \cdot B \\ + \{0.2511 - \cos^2 I \cdot [0.0137 \cdot (1 - \cos(2\alpha)) \\ + 0.1096 \cdot (1 + \cos(2\alpha)) \cdot \sin^2 I]\} \cdot 10^8 \cdot B^2$$

$$1-0: 2 + 0.0913 \cdot 10^8 \cdot B^2$$

$$2-3: 15.68 - 10.08 \cdot \sin^2 I \cdot \cos^2 I \cdot (1 + \cos(2\alpha)) \\ + 0.9633 \cdot 10^4 \cdot \sin I \cdot \cos^2 I \cdot \sin(2\alpha) \cdot B \\ + \{0.7160 - \cos^2 I \cdot [0.0460 \cdot (1 - \cos(2\alpha)) \\ + 0.3682 \cdot (1 + \cos(2\alpha)) \cdot \sin^2 I]\} \cdot 10^8 \cdot B^2$$

$$2-2: 5 + 0.2283 \cdot 10^8 \cdot B^2$$

$$2-1: 0.98 + 0.12 \cdot \sin^2 I \cdot \cos^2 I \cdot (1 + \cos(2\alpha)) \\ - 0.0115 \cdot 10^4 \cdot \sin I \cdot \cos^2 I \cdot \sin(2\alpha) \cdot B \\ + \{0.0447 + \cos^2 I \cdot [0.0005 \cdot (1 - \cos(2\alpha)) \\ + 0.0044 \cdot (1 + \cos(2\alpha)) \cdot \sin^2 I]\} \cdot 10^8 \cdot B^2$$

The magnitude  $B$  of the geomagnetic field is to be entered in Tesla.